

Dynamical synchronization transition in interacting electron systems

Tanay Nag,¹ Robert-Jan Slager,¹ Takuya Higuchi,² and Takashi Oka^{1,3}

¹Max Planck Institute for the Physics of Complex Systems, Dresden 01187, Germany

²Chair of Laser Physics, Department of Physics,

Friedrich-Alexander-Universität Erlangen-Nürnberg (FAU), Staudtstr. 1, D-91058 Erlangen, Germany

³Max Planck Institute for Chemical Physics of Solids, Dresden 01187, Germany

Synchronization is a ubiquitous phenomenon in nature and we propose its new perspective in ultrafast dynamics in interacting electron systems. In particular, using graphene irradiated by an intense bi-circular pulse laser as a prototypical and experimental viable example, we theoretically investigate how to selectively generate a coherent oscillation of electronic order such as charge density waves (CDW). The key is to use tailored fields that match the crystalline symmetry broken by the target order. After the pump, a macroscopic number of electrons start oscillating and coherence is built up through a transition. The resulting physics is detectable as a coherent light emission at the synchronization frequency and may be used as a purely electronic way of realizing Floquet states respecting exotic space time crystalline symmetries. In the process, we also explore possible flipping of existing static CDW orders and generation of higher harmonics. The general framework for the coherent electronic order is found to be analogous with the celebrated Kuramoto model, describing the classical synchronization of coupled pendulums.

Control of quantum matter using non-equilibrium means is an important topic in fundamental science. In ultrafast pump-probe spectroscopy, well-controlled intense lasers are used to induce non-equilibrium phase transitions (reviewed in Refs.¹⁻⁵) and one of the initial ideas was to use the laser excited carriers to trigger a photo-induced insulator-to-metal transition in strongly correlated materials⁶⁻⁸. In this way, it is able to *destroy* orders present in the materials. However, *creating* a non-trivial order is not straightforward. One route is to resonantly pump coherent phonon oscillations optimizing the lattice structure to favor interesting electronic orders⁹⁻¹². Quench induced topological phases would also fall in this category^{13,14}. Another route is Floquet engineering^{15,16}, a control of quantum states by periodic driving, and non-trivial topological states have been proposed¹⁷⁻²¹ and realized²²⁻²⁴. Here, we study a hybrid of these two ideas. Namely, we study how to generate coherent electron oscillations in interacting electron systems with an aim to realize novel Floquet states. To be more specific, we investigate oscillating orders with frequency Ω_0

$$\langle c_a^\dagger(t)c_b(t) \rangle = \Delta_{ab}e^{-i(\Omega_0 t - \phi)} + \dots \quad (1)$$

that did not exist in the groundstate but are created by a short but intense pump laser field. Here, a, b denote the

position (and spin, orbital...) indices and the amplitude Δ_{ab} is at most a slowly changing function. Various oscillations of density waves (CDW, spin density wave, bond density wave etc.) fit into this category. We note that a dynamical order ‘‘Floquet condensation’’ analogous to (1) was also found in strongly interacting gauge theories, but the microscopic understanding of the mechanism is still lacking²⁵.

A desired coherent oscillation can be selectively created by using pump fields that are carefully tailored. This is in contrast to the Higgs amplitude mode²⁶⁻³², *i.e.* a small oscillation of an already existing groundstate order, which can be triggered by a delicate but featureless excitation across the gap. To make the argument solid, we use light irradiated graphene³³ as an example since it is a prime testbed for theoretical and experimental researches^{17,34-38}. We study electrons on the honeycomb lattice at half-filling described by the Hamiltonian

$$H = \frac{1}{N} \sum_{\mathbf{k}\sigma} \hat{\psi}_{\mathbf{k}\sigma}^\dagger \mathcal{H}(\mathbf{k} + \mathbf{A}) \hat{\psi}_{\mathbf{k}\sigma}, \mathcal{H}(\mathbf{k}) = \begin{pmatrix} 0 & h(\mathbf{k}) \\ h(\mathbf{k})^* & 0 \end{pmatrix} \quad (2)$$

with $\hat{\psi}_{\mathbf{k}\sigma}^\dagger = (c_{A\mathbf{k}\sigma}^\dagger, c_{B\mathbf{k}\sigma}^\dagger)$ in the momentum \mathbf{k} space, while A, B are the sublattice indices. $h(\mathbf{k}) = \sum_{l=0}^2 J e^{-i\mathbf{k} \cdot \mathbf{e}_l}$, $\mathbf{e}_l = (\cos \phi_l, \sin \phi_l)$ with $\phi_l = \pi/2 + 2\pi l/3$ sets the hopping and N is the number of unit cells in the lattice. The CDW and complex bond order parameters are

$$\Delta = \frac{1}{N} \sum_{\mathbf{k}} \Delta_{\mathbf{k}}, b^\pm = \frac{1}{N} \sum_{\mathbf{k}} b_{\mathbf{k}}^\pm \quad (3)$$

with $\Delta_{\mathbf{k}} = \sum_{\sigma} \langle [c_{A\mathbf{k}\sigma}^\dagger c_{A\mathbf{k}\sigma} - c_{B\mathbf{k}\sigma}^\dagger c_{B\mathbf{k}\sigma}] \rangle$ and $b_{\mathbf{k}}^{+(-)} = \sum_{\sigma} \langle c_{A(B)\mathbf{k}\sigma}^\dagger c_{B(A)\mathbf{k}\sigma} \rangle$. How can we dynamically induce a CDW oscillation using laser? The order breaks the sublattice symmetry, reducing the lattice’s C_{6v} crystalline symmetry down to C_{3v} . Bi-circular laser, which is itself an experimentally well-established technique³⁹, can be expressed by a gauge field ($A = A_x + iA_y$)

$$A = A_L e^{i\omega t} + A_R e^{-2i\omega t + i\theta} \quad (4)$$

also has this lower C_{3v} symmetry (we set $A_R = A_L$). Under the electric field $E(t) = -\partial_t A$, the A and B sublattices become inequivalent (Fig. 1a) and is expected to trigger the desired oscillation of Δ . A bi-circular laser effectively induces terms that break the C_{6v} symmetry and the Floquet effective Hamiltonian includes a AB-sublattice potential $m_{\text{eff}} \sum_{\mathbf{k}\sigma} [c_{A\mathbf{k}\sigma}^\dagger c_{A\mathbf{k}\sigma} - c_{B\mathbf{k}\sigma}^\dagger c_{B\mathbf{k}\sigma}]$ (see

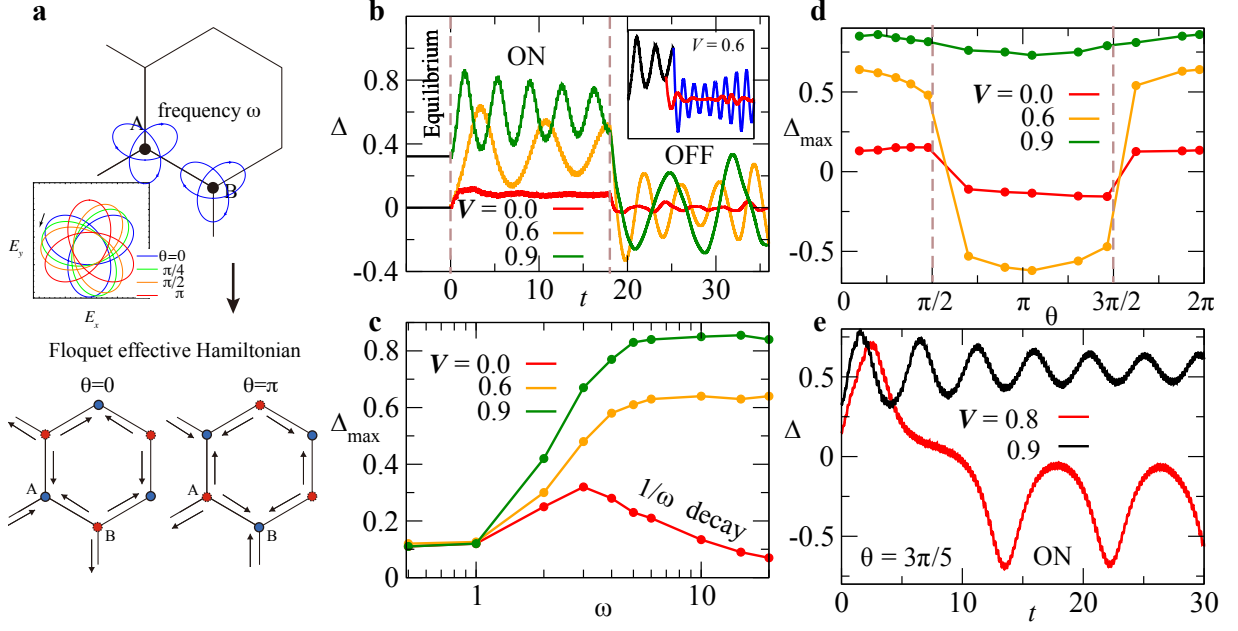


FIG. 1. **Dynamics of CDW oscillation.** **a**, Bi-circular laser field, as depicted by the blue curve, makes the A and B sublattices in the honeycomb lattice are inequivalent (inset: angle dependence). When it is ON, effective terms such as an on-site AB-sublattice alternating potential is dynamically induced, which triggers a charge transfer (arrows). **b**, Time evolution of the CDW order parameter. The oscillation amplitude and the mean values of Δ are both enhanced by the interactions. Inset shows that for a given value of interaction strength ($V = 0.6$), the relaxation dynamics bears a prominent memory effect depending on the values of CDW order particularly at instant when laser field is switched off. ($\omega = 10.5$, $\theta = \pi/10$). **c**, The maximum value of the CDW order Δ_{\max} , during the bi-circular driving, shows a significant increase in the interacting case for $\omega > 2$. ($\theta = \pi/10$). **d**, The dependence of Δ_{\max} on the angle θ of the bi-circular field. It switches sign around $\theta = \pi/2$ and $\theta = 3\pi/2$ ($\omega = 10.5$). **e**, Starting within the CDW phase, it is possible to flip the order when we are near both the phase boundary and $\theta = \pi/2$.

supplementary II B). This can push the electrons from A to B sublattices (or vice versa) initiating the oscillations.

Collective dynamics occur when we add electron-electron interactions

$$H_{int} = \frac{U}{2} \sum_i n_i n_i + V \sum_{\langle i,j \rangle} n_i n_j \quad (5)$$

to the free Hamiltonian (2), where U and V denote the on-site and nearest neighbor Coulomb repulsion respectively ($n_i = \sum_{\sigma} c_{i\sigma}^{\dagger} c_{i\sigma}$, $\langle i,j \rangle$: nearest neighbor pairs). The real time dynamics of the extended Hubbard model at half-filling on the honeycomb lattice is studied within the time-dependent mean-field approximation using

$$\mathcal{H}_{MF}(\mathbf{k}) = \frac{1}{2} \begin{bmatrix} (\frac{U}{2} - 3V)\Delta & 0 \\ 0 & -(\frac{U}{2} - 3V)\Delta \end{bmatrix} + \mathcal{H}(\mathbf{k}) + \left(\frac{U}{4} - \frac{3V}{2}\right)I \quad (6)$$

to govern the time evolution. Below, we set $J = 1$ to fix the energy scale and use $A_R = A_L = 1$. Since the combination $U/2 - 3V$ is the only relevant interaction parameter within this approximation, we set $U = 0$ and use V as the parameter representing the correlation effect. Within the mean field approximation, the critical

value for the groundstate CDW transition is $V_c = 0.78$. In graphene³³, the material parameters are known to be close but below the critical value accommodating a semi-metallic phase⁴⁰.

CDW oscillation and flipping

Figure 1b shows the time evolution of the CDW order triggered by the bi-circular pulse field (4). The field is suddenly ramped up and down at the beginning and end of the ON region. We checked that the findings qualitatively remain unaltered for slow ramping protocols. Interactions substantially affect the CDW order. They give rise to a pronounced oscillation both in the ON and OFF region, where the amplitudes are controlled by the new energy scale set by V . Inset shows that even for the same interaction and pulse strength, the oscillation amplitude of Δ during the relaxation dynamics significantly depends on the value of Δ at which the field is switched off. This memory effect (or initial value effect) is completely absent for the non-interacting case. In Fig. 1c, we further investigate ω and V dependence of Δ_{\max} . The first observation is that CDW oscillations can be induced in a wide range of pump frequencies. However, a strong upturn occurs when $\omega = 2$ is exceeded. This is also where

the interaction starts to assist the oscillation. For higher ω , we find that Δ_{\max} saturates for the interacting case, in contrast to the non-interacting case, where Δ_{\max} falls off as $1/\omega$, following high frequency perturbation theory (see Supplementary II).

The angle θ of the applied bi-circular field plays a crucial role in controlling the CDW order (see Fig. 1d). For $\theta = 0, \pi$, it induces an effective AB-sublattice potential that favors a CDW order, and Δ_{\max} becomes largest with opposite signs as shown in Fig. 1d. Flipping of already existing CDW order is possible (Fig. 1e). We find that Δ can be flipped when we start in the ordered phase but not so far from the phase boundary. As for the direction of the bi-circular field, the flipping started to occur above $\theta = \pi/2$ and became maximum around $3\pi/5$. Although we don't have a clear understanding of the flipping mechanism yet, at least in the non-interacting case, we find an analogous picture to the spin-echo (π -pulse) technique in NMR. Specifically, if we view the effective Floquet Hamiltonian (see supplementary II) as a spin Hamiltonian $\mu \mathbf{B}_{\mathbf{k}} \cdot \boldsymbol{\sigma}$, the order parameter Δ is analogous to a z -direction magnetization. The situations for $\theta = 0, \pi$ correspond to having a z -field since an effective AB-sublattice potential is induced and tries to align the spin in the z -direction. However, once the order is established, a z -magnetic field that commutes with the order is not able to change it. On the other hand, the $\theta = \pi/2$ situation corresponds to having a transverse field, and it can be used to rotate the existing order Δ by suitably tuning σ_x and σ_y components in the effective Hamiltonian (see supplementary II).

Synchronization order parameter

Density oscillations are usually quickly damped due to dephasing because electron-hole pair excitations, created by short and intense fields, spread out broadly in the energy-frequency space⁴¹. *Dynamical synchronization transition* (DST), ubiquitous in non-linear dynamical systems, is a mechanism that acts against dephasing^{42,43}. An ensemble of interacting oscillators with different frequencies can oscillate collectively at a single synchronization frequency Ω_0 . In the present system, the momentum-resolved CDW, current, and bond order parameters ($\{\Delta_{\mathbf{k}}, J_{\mathbf{k}} = -i(b_{\mathbf{k}}^+ - b_{\mathbf{k}}^-), K_{\mathbf{k}} = (b_{\mathbf{k}}^+ + b_{\mathbf{k}}^-)\}$) define a three dimensional vector field in the Brillouin zone. We find below that, while $K_{\mathbf{k}}$ changes only slowly, the $(\Delta_{\mathbf{k}}, J_{\mathbf{k}})$ component rotates around the $K_{\mathbf{k}}$ -axis swiftly (with natural frequency $\Omega = 2|h(\mathbf{k})|$ in the non-interacting case) and plays the role of the angle in the classical oscillator synchronization problem. The angle $\gamma_{\mathbf{k}}$ specifying the $(\Delta_{\mathbf{k}}, J_{\mathbf{k}})$ direction can be thought of as a generalized polarization direction. We can define^{42,43} the collective phase ψ and amplitude r by

$$r e^{i\psi} = \frac{1}{N} \sum_{\mathbf{k}} e^{i\gamma_{\mathbf{k}}}, \quad e^{i\gamma_{\mathbf{k}}} = -\frac{\Delta_{\mathbf{k}} + iJ_{\mathbf{k}}}{|\Delta_{\mathbf{k}} + iJ_{\mathbf{k}}|}. \quad (7)$$

The amplitude $r \in [0, 1]$ plays the role of the synchronization order parameter, and gives the fraction of the

synchronized oscillators. For example, $r = 1$ ($r = 0$) means full (no) synchronization is achieved. A non-zero r signals a transition from a dephased state to a coherent one.

Direct evidence for DST can be obtained by evaluating the average value synchronization order parameter r_{av} as shown in Fig. 2a, where we do the time average in the OFF region for a considerably long time span ($15 < t < 200$). As the interaction is increased, the synchronization order parameter increases monotonically, and we find a singular upturn associated with a non-analytic behavior signifying a collective transition. This transition is dynamical in the sense that it depends on how the CDW order is induced. For example, the critical interaction strength, referred as V_{DST} , depends on the details of driving i.e., the frequency ω and field strength $A_L = A_R$ of the bi-circular field as well as details of the underlying lattice model. An interesting observation is that r_{av} is non-zero even for the non-interacting case. This is due to the van Hove singularity in the density of states (DOS) at $\varepsilon_{\text{vH}} = \pm 1$ for the honeycomb lattice, representing a large fraction of coherent electron-hole pairs at $\Omega_0 = 2 = 2|\varepsilon_{\text{vH}}|$. In order to isolate this effect, we study the DST by using a modified lattice Hamiltonian with smoothed and broadened DOS without a singularity (see Fig. 2b). There we find that r_{av} in the non-synchronized phase stays at a smaller value approaching zero under a scaling analysis (as $N^{-1/2}$), and the transition becomes much more sharp and pronounced (see supplementary I).

We can obtain a deeper understanding of DST by looking into momentum resolved synchronization correlation defined by ($t_i = 15, t_f = 50$)

$$S_{\mathbf{k}} = \frac{1}{\delta t} \int_{t_i}^{t_f} \Delta(t) \Delta_{\mathbf{k}}(t) dt \quad (8)$$

plotted in Figs. 2c, d. While the correlation is very weak in the non-interacting case, we see significant correlation built up in the interacting case in a red patch around the equal energy ($2|h(\mathbf{k})| = \text{const.}$)-contours close to the van-Hove singularity (blue dashed contour in Fig. 2d). The synchronization of the momentum modes can thus be depicted as the red region in Figs. 2f by rotors rotating with a common phase $\gamma_{\mathbf{k}} \sim \psi$, while green region illustrates the incoherent non-synchronized case. Physically, the momentum resolved order $(\Delta_{\mathbf{k}}, J_{\mathbf{k}})$ is associated to electron-hole pair excitation with energy $E_e - E_h \simeq 2|h(\mathbf{k})|$. Then moving to the energy ε space, we can think of an intuitive picture as shown in Figs. 2e. The pulse field excites electron-hole pairs with a broad distribution in energy space. Their polarization (designated by an arrow) start to rotate individually with frequencies $\simeq 2|h(\mathbf{k})|$. Below the DST transition ($V < V_{\text{DST}}$), they keep rotating incoherently and average out to zero. While above the DST ($V > V_{\text{DST}}$), coherence among the electron-hole pairs is established collectively through interaction. The degree of synchronization is increased when the electron-hole pair density

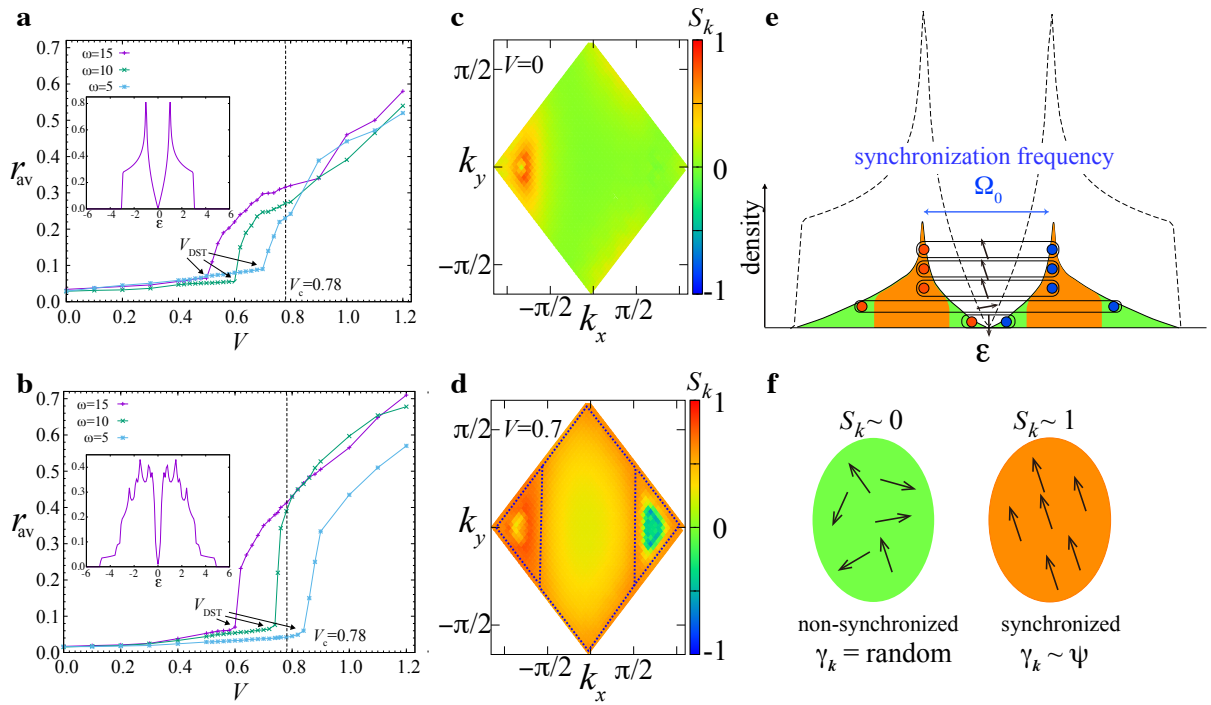


FIG. 2. **Dynamical synchronization transition.** **a**, The synchronization order parameter (average value) r_{av} for the model on a honeycomb lattice ($\theta = \pi/10$, $N = 100 \times 100$). Inset shows the density of states. V_{DST} is the critical interaction strength for the DST to occur. **b**, Same as **a** but with an altered lattice model having a reduced singularity in its density of states. **c**, **d**, Momentum resolved synchronization correlation $S_{\mathbf{k}}$ for $V = 0.0$ and $V = 0.7$, respectively. ($\omega = 10$, $\theta = \pi/10$). Blue dotted line in **d** shows the contour $|h(\mathbf{k})| = 1$ signifying the van-Hove singularity. **e**, Schematic plot of the electronic density of states (dashed) in the honeycomb lattice and the distribution of electron-hole pairs (solid). The latter is closely connected to $\int d^2\mathbf{k} |\Delta_{\mathbf{k}} + iJ_{\mathbf{k}}| \delta(\epsilon - |h(\mathbf{k})|)$ and quantifies excitations due to pumping in the presence of interaction. The blue and red circles represent electron-hole pairs and the arrow refers to their polarization direction $\gamma_{\mathbf{k}}$. **f**, Green and red regions schematically depict the non-synchronized and synchronized states respectively in momentum (**c**, **d**) and energy (**e**) spaces. The arrows illustrate $\gamma_{\mathbf{k}}$ and in the synchronized state, they rotate with a synchronization frequency Ω_0 and its direction defines the collective phase $\gamma_{\mathbf{k}} \sim \psi$.

becomes higher. The synchronization frequency Ω_0 depends on the excitation distribution and its value is close to peak of the above distribution. Even in the synchronized state, there can be non-synchronized excitations associated with energies away from $\hbar\Omega_0$.

The mathematical structure behind the DST can be elucidated as we can relate the time evolution within the mean field approximation (6) to a variant of the Kuramoto model^{42,43} that governs the dynamics of $\gamma_{\mathbf{k}}$ (supplementary I). The mean field coupling can be mapped to the synchronization force and the laser pumping to an external force. This framework is general and applies not only to graphene but to wide variety of correlated electron systems even without the van-Hove singularity and to their collective dynamics.

Coherent light emission and HHG

How can we experimentally verify the DST? While the CDW is not easily accessible, currents induced by a laser can be measured directly as shown by recent work^{38,44} on high harmonic generation (HHG) in

graphene. Accordingly, we now investigate the non-equilibrium evolution of the induced current ($J_a = \sum_{\mathbf{k}\sigma} \psi_{\mathbf{k}\sigma}^\dagger [\partial\mathcal{H}(\mathbf{k} + \mathbf{A})/\partial k_a] \psi_{\mathbf{k}\sigma}$) as depicted in Fig. 3a. The current shows a prominent beating pattern with increasing V in both ON and OFF regions. This beating reflects the CDW oscillation already presented in Fig.1, as the current reflects the movement of charge between the A and B sublattices. Most interestingly, in the ON region, we observe the generation of higher harmonics i.e. output frequency $\Omega = n\omega$ while investigating the Fourier component of the current (see Fig. 3b).

Concentrating on the OFF region, an oscillation with more prominent coherence in J_y is observed for V near V_c . A large peak at $\Omega_0 \sim 1.5$ is present in the Fourier spectrum of J_y (Fig. 3c). The synchronization frequency Ω_0 is selected dynamically through a correlation effect and depends strongly on the electron-hole pair population density as we discussed after Fig. 2e. The synchronization frequency Ω_0 is red shifted from the van-Hove singularity $\Omega_{vH} = 2$. This is because the electron-electron repulsion V , which is attractive between electrons and holes,

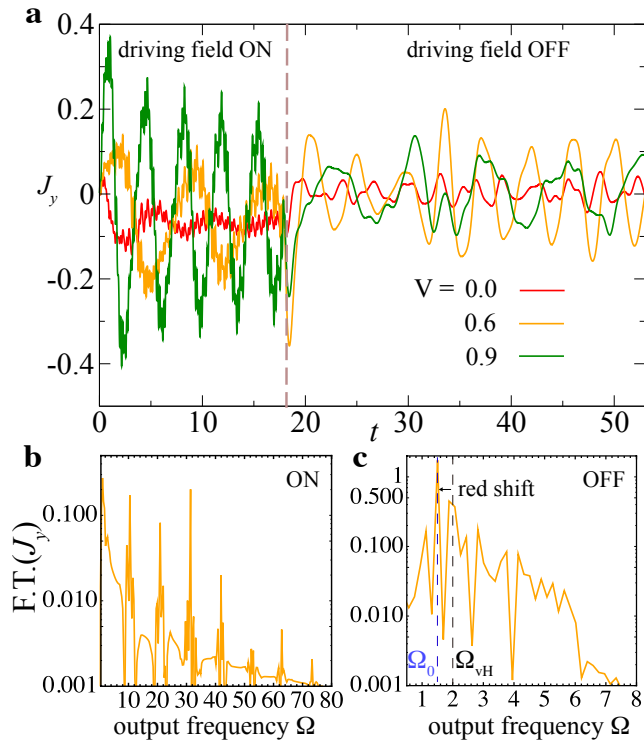


FIG. 3. **Possible experimental observation in the current.** **a** The time evolution of the current for the same parameters as Fig. (1b). The Fourier transform of J_y in the **(b)** ON and **(c)** OFF regions. **b** Generation of higher harmonics is observed in the ON region. **c** In the OFF region, the synchronization frequency of the oscillation shows a red shift from the van Hove singularity ($\Omega_{\text{vH}} = 2$) due to correlation effect to $\Omega_0 \simeq 1.5$. For **b** and **c** $V = 0.6$ is used, while $\theta = \pi/10$, $\omega = 10.5$ is used for all plots.

reduces the pair energy from the bare value $2|h(\mathbf{k})|$ by its binding energy. There has been an optical luminescence experiment in graphene and the luminescence peak is found at 4.62 eV which is reduced from the expected bare van-Hove energy 5.2 eV⁴⁵.

Road to self-maintained Floquet crystalline states

What is the consequence of having an oscillating mean field? An important point is that Floquet states are now self-maintained by the electronic degrees of freedom. They can remain even after the pump is finished as long as the oscillation exists. The Floquet state realized by DST has a crystalline symmetry now elevated to a space-time crystalline symmetry. For example, an oscillating CDW $\Delta = \Delta_0 \sin \Omega_0 t$ realizes a state with a time-glide symmetry. The mirror symmetry M for the mirror plane along the x -axis between the AB sites is broken by Δ , but a time-glide symmetry $H(t, \mathbf{r}) = MH(t + T/2, \mathbf{r})M^{-1}$ ($T = 2\pi/\Omega_0$) is satisfied. To make this more specific, we considered the generation of such a naturally induced time glide symmetry and its topological aspects in the Floquet condensation picture explic-

itly (see Supplementary III). Indeed, by reverting to the minimal model introduced above, introduction of an oscillatory CDW term in the Hamiltonian can be shown to result in special edge states specific to Floquet states²¹ for different parameter regimes. These edge states at the π -gap in the quasi energy spectrum persist until the gap is closed and are related to the chiral symmetry of the system⁴⁶. Nonetheless, while this is a particular example of a topological symmetry protected state, this mechanism in general opens the door to access many new topological phases protected by new symmetries. Parallel to how the concept of topological insulators^{47,48} is upgraded to topological crystalline insulators⁴⁹⁻⁵³, the notion of Floquet topological insulators^{17,18} can be refined by considering the space-time crystalline symmetry⁵⁴. The DST, with the above example in particular, thus provides an experimentally viable route to realize long lived Floquet topological crystalline insulators⁵⁵.

Another important point is the possibility of phason modes ϕ in Eq. (1). Windings can exist due to the equivalence $\phi(\mathbf{x}) \sim \phi(\mathbf{x}) + 2\pi$, leading to topological excitations. Examples include vortices and domain walls, which should bind non-trivial defect or edge modes similar to their static counterparts in Floquet topological crystalline insulators^{56,57}. We will report on these issues elsewhere.

Beyond mean field

Before closing, let us comment on the validity of our prediction which is based on the time dependent mean field approximation. In real materials, relaxation due to phonons as well as electron-electron scattering processes are important. In particular, in graphene, it is known that phonon emission is the dominant relaxation channel, and the typical time scale for this to happen is few hundred femtoseconds (fs)⁵⁸. On the other hand, in our simulations, the unit of time is 1.8 fs considering the tunneling amplitude $J = 2.3$ eV for graphene. Thus, the synchronization oscillation period $T = 2\pi/\Omega_0 \simeq 8$ fs is well shorter than the relaxation time scale. As for electron-electron scattering process, considering the effect of a momentum-time dependent random mass term that mimics scattering, we find that the coherence persists up to a certain realistic disorder strength (supplementary IV). In addition, heating may take place in the ON region. However, our protocol uses short pulse excitation and we think that heating is not a severe problem in observing DST. This is because it is known that there exists a Floquet-prethermalization time scale below which the heating is negligibly small^{59,60}.

Conclusion

There exists a plethora of studies on Floquet topological insulators in the condensed matter community, but up to now, the exciting topological features have been limited in time by the duration of laser pulse. We introduced the concept of DST in a simple setup, where a tailored laser pulse is used to induce a collective elec-

tronic order dynamically. We find that DST paves the way to realize a Floquet topological state that is self-maintained and may become considerably long lived. In addition, DST gives a microscopic foundation to Floquet condensation Eq. (1) as discussed in a holographic Floquet system²⁵. Our findings also include general measurable features such as coherent light emission and HHG, as well as a realistic protocol to flip and control CDW orders.

Appendix

In this Appendix we comment on the numerical details underlying the results of the main text. Moreover, we reveal the analogy between Kuramoto model and the graphene under bi-circular laser field. In particular, we show that the two level problem can be mapped to an effective Kuramoto model which qualitatively describes the synchronization phenomena occurring in charge density wave order in the presence of interactions. We also compare these results with the non-interacting case. Simultaneously, we try to motivate a more physical picture of the synchronization process using charge density wave order, current order and bond order. We then consider another honeycomb lattice model with an additional hopping term to investigate the dynamical synchronization transition (DST) more critically. We find that singularity in the density of states is not a necessary condition to have DST. We extend our results in the context of Floquet perturbation theory to show that in the high frequency limit an inversion symmetry breaking mass term indeed generated. We also study the effective hopping terms individually to understand the dynamical behavior of charge density wave order in an extensive way. After that, we use the effective model to illustrate the emergence of edge states in case of an oscillating CDW term that generates a time glide symmetry. This shows that in a Floquet condensation picture, DST setups can be used to access new symmetry protected topological phases. Finally, we consider a random momentum-time mass term to study the scattering effect on the synchronization where we show that substantial disorder can destroy the DST. We further comment on the heating mechanism during the driving and its impact on DST.

Appendix A: Numerical Details

We here would like to mention a few technical detail to calculate the CDW order in presence of interaction. We consider the momentum space 2-level graphene Hamiltonian (2) to carryout the time-dependent mean field treatment. First, we determine the initial value of ρ_A and ρ_B , before going into dynamics, by an iterative method for a given value of U and V ; in order to this, we consider some random initial guess for ρ_A and ρ_B . Once Δ is set in such a way, we proceed with time dependent Schrödinger equation, governed by the Hamiltonian $\mathcal{H}_{\text{MF}}(\mathbf{k})$ (Eq. 6) and solved it again iteratively using the forth order Runge-Kutta method. In the switch ON region with an explicit time dependence Hamiltonian, we continue the iterative

method replacing ρ_A and ρ_B at every steps of time with their updated values as mean field results in a dynamical evolution of ρ_A and ρ_B . In the switch OFF region, the same process continued without the explicit time dependence of the Hamiltonian.

Appendix B: On the dynamical synchronization transition

1. Time dependent mean field approximation and a link to Kuramoto physics

Here, we outline the connection between the dynamics, based on the time dependent mean field approximation, and the Kuramoto model, describing the synchronization transition for coupled pendulum. In order to simplify the argument, let us incorporate the effect of the bi-circular laser field by an effective AB-sublattice alternating potential $m_A = m_0$, $m_B = -m_0$, which is justified using the high frequency expansion (supplementary II). The model Hamiltonian then reads

$$H_k(t) = \begin{bmatrix} \lambda\Delta(t) + m_0 & h_k \\ h_k^* & -\lambda\Delta(t) - m_0 \end{bmatrix} \quad (\text{B1})$$

with the mean field potentials $\lambda\Delta(t)$ and $\Delta(t) \equiv \sum_{\mathbf{k}} \rho_{\mathbf{k}}^A(t) - \rho_{\mathbf{k}}^B(t)$, where $\lambda = 1/2(U/2 - 3V)$. Using unitary transformations $U_1 = \exp(-i\sigma_z\phi_k/2)$, $U_2 = \exp(-i\sigma_y\pi/4)$ with $\phi_k = \text{Arctan}(\text{Im}(h_k)/\text{Re}(h_k))$, we re-express the Hamiltonian in a more convenient rotated basis⁶¹

$$\hat{H}_k(t) = U_2 U_1 H_k(t) U_1^\dagger U_2^\dagger = \begin{bmatrix} |h_k| & \lambda\Delta(t) + m_0 \\ -\lambda\Delta(t) - m_0 & -|h_k| \end{bmatrix}. \quad (\text{B2})$$

In this basis, the charge density order becomes $\Delta(t) = -2 \sum_{\mathbf{k}} \text{Re}(u_k^* v_k)$, where $u_k(v_k) = 1/\sqrt{2}(+(-)) \exp(-i\phi/2)\psi_k^A + \exp(i\phi/2)\psi_k^B$. The mean field equation of motion governing the dynamics can be recasted as follows

$$i\dot{w}_k = 2|h_k|w_k + (\lambda\Delta(t) + m_0)(w_k^{-1} - w_k)w_k, \quad (\text{B3})$$

where $w_k = u_k/v_k$.

Next, we rewrite this equation using the polarization angle γ_k using $u_k = \cos\theta_k \exp(i\gamma_k^1)$ and $v_k = \sin\theta_k \exp(i\gamma_k^2)$ under the condition of $|u_k|^2 + |v_k|^2 = 1$. This leads to $\Delta(t) = -\sum_p \sin(2\theta_p) \cos\gamma_p$, $\gamma_p = \gamma_p^1 - \gamma_p^2$. One can readily show from Eq. (B3) that

$$\begin{aligned} \dot{\gamma}_k w_k - i \frac{2}{\sin(2\theta_k)} \dot{\theta}_k w_k &= 2|h_k|w_k - 2w_k \lambda \sum_p \sin(2\theta_p) \cot(2\theta_k) \cos\gamma_p \cos\gamma_k + 2iw_k \lambda \sum_p \frac{\sin(2\theta_p)}{\sin(2\theta_k)} \cos\gamma_p \sin\gamma_k \\ &+ 2m_0 w_k [-\cot(2\theta_k) \cos\gamma_k + i \frac{\sin\gamma_k}{\sin(2\theta_k)}] \end{aligned} \quad (\text{B4})$$

This further simplifies to two coupled first-order differential equations in θ_k and γ_k given by

$$\begin{aligned} \dot{\gamma}_k = & 2|h_k| + 2\lambda \sum_p \sin(2\theta_p) \cot(2\theta_k) \times [\cos(\gamma_p - \gamma_k) \\ & + \cos(\gamma_p + \gamma_k)] - 2m_0 \cot(2\theta_k) \cos \gamma_k \end{aligned} \quad (\text{B5})$$

and

$$\dot{\theta}_k = (-m_0 + \lambda \sum_p \sin(2\theta_p) \cos \gamma_p) \sin \gamma_k \quad (\text{B6})$$

On the other hand, the generalized Kuramoto model^{62–66} is represented by

$$\dot{\eta}_i = \omega_i + \sum_{j=1}^N M_{ij} \sin(\eta_i - \eta_j) + \epsilon_i(t) + F \sin(\sigma t - \eta_i) \quad (\text{B7})$$

which governs the synchronization between N coupled (with coupling parameter M_{ij}) phase oscillators with phases η_i , oscillating with individual frequency ω_i . The F term represents the forcing strength. ϵ_i is a noise term that represents coupling to fast random degrees of freedom that leads to dissipation.

Comparing Eq. (B5) and Eq. (B7), one can infer that γ_k plays the role of η_i in the Kuramoto model, and $2|h_k|$ of ω_i . From our numerical results, $\cos(\gamma_p + \gamma_k)$ in Eq. (B5) oscillates very fast and mimics the noise term ϵ_i . When the laser field is on ($m_0 \neq 0$), the last term of Eq. (B5) tries to pin the phases, and thus, corresponds to the forcing term in the Kuramoto model with $\sigma = 0$. The coupling M_{ij} is related to the $\lambda \sin(2\theta_p) \cot(2\theta_k)$ factor. This tells us two things. First, from the interaction dependence of the transition as shown in Fig.2 a in the main text, we notice that $\lambda (= 1/2(U/2 - 3V))$ is the key resource for connecting different k modes leading to the DST. Second, the memory effect as shown in the inset of Fig.1 b (main text) can be understood by the $\sin(2\theta_p) \cot(2\theta_k)$ -term. If we switch off the field when this term is small, the DST transition may not occur even when λ is sufficiently large.

The synchronization order parameter for the Kuramoto model defined by

$$r \exp(i\psi) = 1/N \sum_j \exp(i\eta_j) \quad (\text{B8})$$

is evaluated numerically from our data in momentum space k by $r = \sqrt{(\sum_k \sin \gamma_k)^2 + (\sum_k \cos \gamma_k)^2}/N$ and $\psi = \text{Arctan}(\sum_k \sin \gamma_k / \sum_k \cos \gamma_k)$.

We note that the mean field equations Eq. (B5) and Eq. (B6) can also be expressed in terms of the momentum resolved CDW Δ_k , current J_k and bond order K_k parameters. The three dimensional vector field in the momentum BZ are given by $\{\Delta_k, J_k, K_k\} = \{-\sin 2\theta_k \cos \gamma_k, -\sin 2\theta_k \sin \gamma_k, \cos(2\theta_k)\}$. With the new variables, $\tan \gamma_k = J_k/\Delta_k$, $\tan 2\theta_k = \sqrt{J_k^2 + \Delta_k^2}/K_k$, 0 we can show (neglecting the \dot{K}_k

term since K_k evolves slowly) that the mean field equations can be recasted into

$$\begin{aligned} \dot{\Delta}_k = & -h_k J_k - \frac{2}{\Delta_k^2 + J_k^2} [m_0 J_k (K_k J_k + \frac{\Delta_k}{K_k}) \\ & + \lambda \Delta_k J_k \sum_p \frac{\Delta_p}{N} (K_k + \frac{1}{K_k})] \end{aligned} \quad (\text{B9})$$

$$\begin{aligned} \dot{J}_k = & h_k \Delta_k + \frac{2}{\Delta_k^2 + J_k^2} [\lambda \sum_p \frac{\Delta_p}{N} (K_k \Delta_k^2 - \frac{J_k^2}{K_k}) \\ & - 2m_0 J_k (\frac{J_k}{K_k} - K_k \Delta_k)] \end{aligned} \quad (\text{B10})$$

This expression highlights the interplay between current and CDW order.

Moreover, we stipulate that in the weak interacting limit ($\lambda \ll 1$) our model may lead to chaos. This is because there are some literatures^{67–69} studying the Kuramoto models that reports the existence of the chaotic regime. We will report on this aspect elsewhere.

2. Investigating DST critically

Effect of the van-Hove singularity: In order to investigate DST more clearly, we shall consider two lattice models (i) graphene (ii) graphene with an additional AB hopping terms, both in the honeycomb lattice geometry. The motivation behind considering this extra lattice model is that to identify the influence of van-Hove singularity in the DST. The additional off-diagonal hopping term $\sin(k_x - k_y) \cos(k_x + k_y)$ is able to reduce the van Hove singularity of the density of states as shown in the main text.

We study the time evolution for synchronization order parameter r for these above two models. The common findings observed in both the models are the following: Starting from the non-ordered state ($V < V_c$), the order parameter r starts from zero because the phase is indefinite, and increase quickly as the field activates the oscillation in the ON region. r starts from unity if the groundstate is ordered. Prominent interaction dependence shows up in the switch OFF region. As the interaction is increased, the time averaged synchronization order parameter increases monotonically. In the ON region, r stays at a higher value compared to that in the OFF region. This reflects the fact that driving enhances the degree of synchronization and this is again related to the generation of more electron-hole pairs during the driving. Now, the marked difference between them is that for $V = 0.7$, model (ii) with additional hopping does not show any trace of synchronization transition while model (i) already experiences the DST i.e., r stays positive well above zero in the OFF region. Therefore, it is evident that the DST is not only depends on the external driving but also on the specific details of the model. The interesting point is that upon the inclusion of $\sin(kx - ky) \cos(kx + ky) (c_{A\mathbf{k}\sigma}^\dagger c_{B\mathbf{k}\sigma} + c_{B\mathbf{k}\sigma}^\dagger c_{A\mathbf{k}\sigma})$ term,

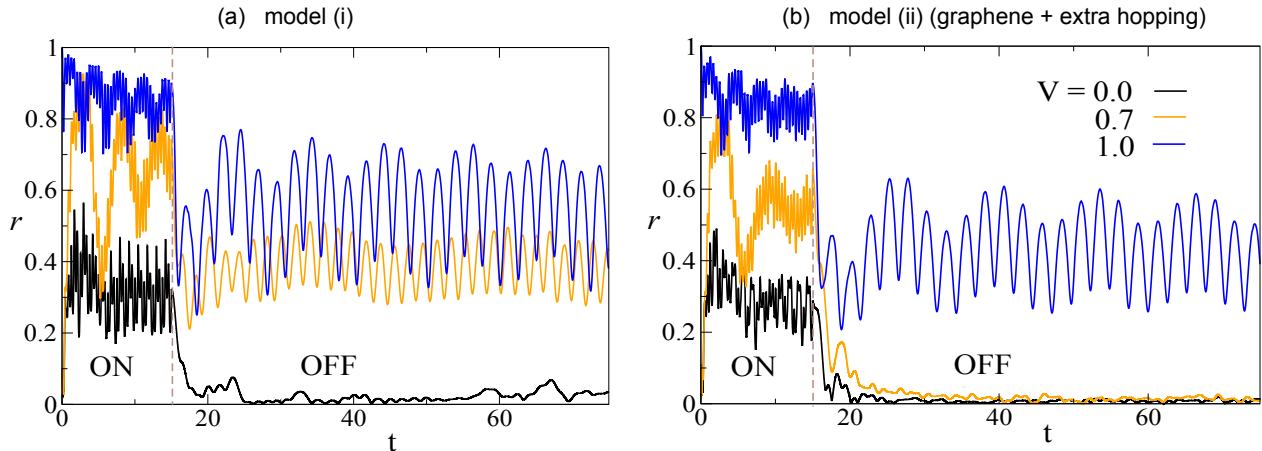


FIG. 4. Time evolution of synchronization order parameter r for graphene, model (i) (a), and graphene with additional hopping i.e., model (ii) (b). We consider $\theta = \pi/10$ and $\omega = 10$ and $N = 100 \times 100$.

the van-Hove singularity is reduced and the density of states (DOS) gets smoothed and broadened. This has its impact on r in the switch OFF region where r continues staying in a much less values compared to model (i). This effect is clearly visible in Fig. 2 of the main text where r_{av} is plotted against V to show the DST in a more generic way. We use this data to calculate the average value of r , r_{av} as shown in the Fig. 2 of the main text.

The striking difference between these two models is that the jump in r_{av} for model (ii) while undergoing a DST is much more than that of the for model (i). Therefore, the singularity in DOS yields some trivial synchronization even in the non-synchronized phase where interaction is not able to initiate a collective phenomena. This results in a relatively high value of r_{av} in the above phase. While in the synchronized phase, the interaction plays the key role over the trivial synchronization factor. On the other hand, for model (ii), trivial synchronization is irrelevant and V plays the pivotal role. As a result, difference between the values of r_{av} in synchronized and non-synchronized phase is larger for model (ii) as compared to model (i). Consequently, a clear sharp and singular upturn is observed for model (ii) in Fig. 2b of the main text.

Scaling analysis: Having described the DOS dependence on r_{av} , we shall now numerically try to establish the dynamical synchronization transition in a more concrete way by investigating the system size scaling properties of r_{av} . We first check the behavior for larger system size in honeycomb graphene lattice model (i). For that, we set $V = 0.4$ in the non-synchronized regime and $V = 0.9$ in the synchronized regime with $\omega = 10$. We obtain a power law dependence of r_{av} on the system size

$$r_{av} = a_0 + bN^{-1/2} \quad (\text{B11})$$

in both the regimes (see Figure 5). The $N^{-1/2}$ -scaling

is the same as the Kuramoto model^{65,66}. Interestingly, the $N \rightarrow \infty$ value of r_{av} i.e., a_0 becomes very small ($O(10^{-2})$) for $V = 0.4$ as compared to $V = 0.9$. For the synchronized regime, $a_0 \simeq 0.26$ which now conveys that the synchronization transition is more clearly visible as we approach the thermodynamic limit. For validating our claim in a generic situation where the DOS is broadened and smoothed, we similarly investigate the model (ii). We find the same $N^{-1/2}$ scaling in both synchronized and non-synchronized regimes with $a_0 \simeq 0.50$ and $O(10^{-2})$, respectively.

Synchronization correlation for model (ii): We further study the synchronization correlation $S_{\mathbf{k}}$ for model (ii) to investigate the location of synchronized region the momentum space (see Fig. 6). For the non-interacting case, the rotors (i.e., $\gamma_{\mathbf{k}}$), rotating randomly, are not able to generate any synchronized motion from any part of the momentum space (see Fig. 6 a). This is in contrast to the case with model (i) where some momentum modes near the van-Hove singularity actively participate in the synchronization leading to an enhancement in r_{av} even in the non-synchronized phase. The interacting case with $V = 0.9$ for model (ii) is shown in Fig. 6b. We find a strong synchronized region (red patch) around the left Dirac point K and in the energy space, this corresponds to the $\varepsilon \sim \pm 1.5$ line in DOS for model (ii) (as shown in the inset of Fig. 2 b in the main text). This refers to the fact that even when the singularity is absent, a peak in the density of states is enough to trigger the DST. We note that the K (left) and K' (right) points act differently in the $S_{\mathbf{k}}$ -plot. This is because the bi-circular laser field acts in-equivalently to the two Dirac cones as explained in supplementary II.

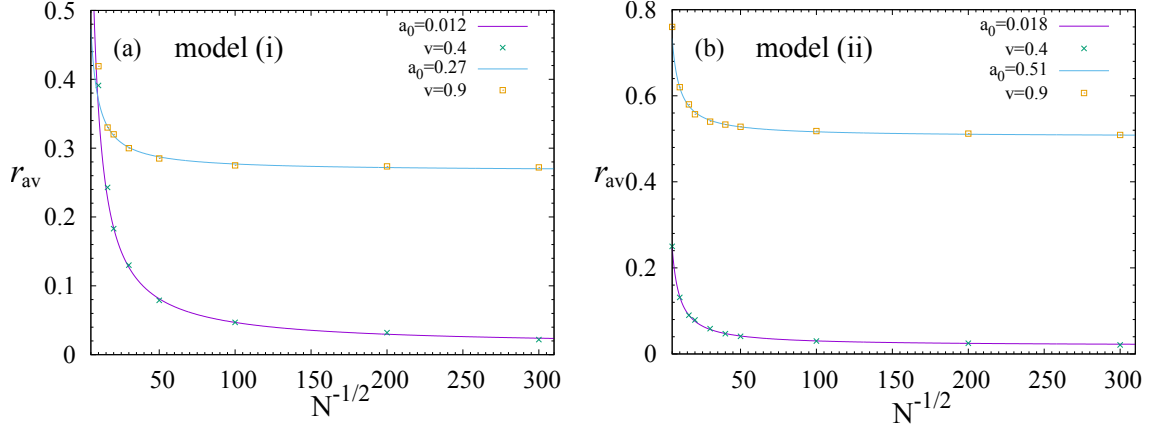


FIG. 5. (a) The plot shows that r_{av} , obtained for model (i), follows a power law scaling: $r_{av} = a_0 + bN^{-1/2}$. Two distinct saturation values as captured by a_0 clearly suggests that there is synchronization transition. Plot (b) is the same as (a) but for the model (ii).

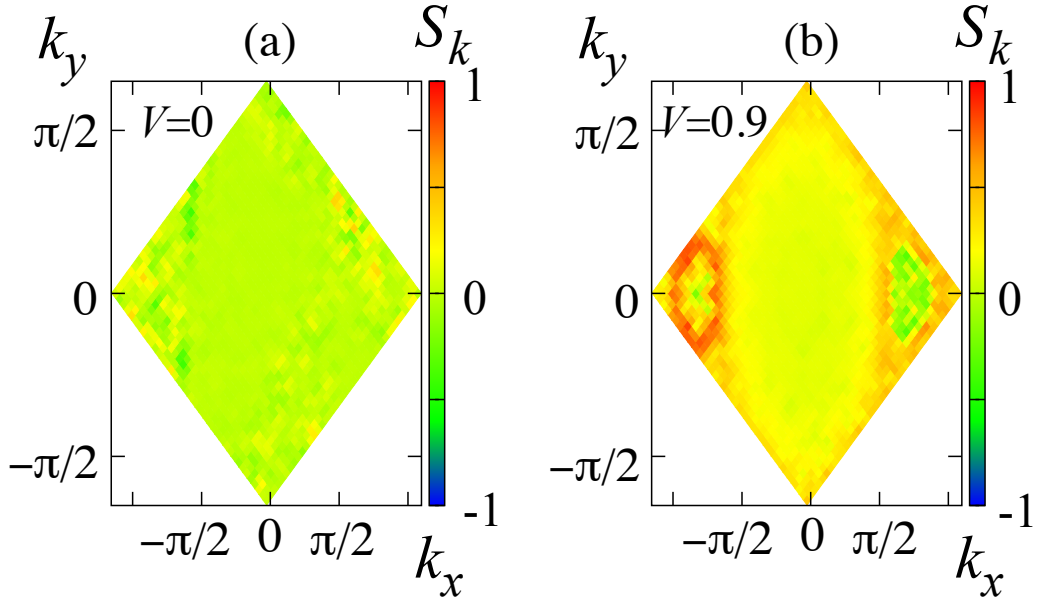


FIG. 6. The momentum resolved density plot of $S_{\mathbf{k}}$ for model (ii) are shown in (a) with $V = 0$ and (b) with $V = 0.9$. The non-interacting case does not exhibit any sign of correlation in the whole BZ while for the interacting case, a strong correlation is built up close to equi-energy surface enclosing Dirac point K.

Appendix C: Floquet dynamical setup

1. Quasi-energy

Let us explain the Floquet quasi-energy spectrum^{17,18,70–72} of our model in the presence of bi-circularly polarized laser field. The Floquet Hamiltonian acting on the Fourier components of the Floquet

state takes the form

$$\mathbf{H} = \begin{pmatrix} \ddots & \vdots & \vdots & \vdots \\ \cdots & \hat{H}_0 - \omega & \hat{H}_1 & \\ & \hat{H}_{-1} & \hat{H}_0 & \hat{H}_1 \\ & & \hat{H}_{-1} & \hat{H}_0 + \omega & \cdots \\ \vdots & \vdots & \vdots & \vdots & \ddots \end{pmatrix},$$

with $\hat{H}_n = \frac{1}{T} \int_0^T \hat{H}_k(t) e^{it\omega n} dt$. Here, $H_k(t)$ is the time dependent lattice Hamiltonian as given in Eq. (2) of the

main text.

We investigate the behavior of quasi-energy as function of k_x with $k_y = 0$ as shown in Fig. (7). The gap at $K = (K, 0)$ can be tuned by varying the frequency and amplitude. The gap at the other Dirac point $K' = (-K, 0)$ does not change significantly. The two quasi-energies of two states residing in the same photon sector or in two consecutive time BZs come closure for low amplitude and low frequency. The relative phase θ is able to tune both the gaps appearing at the Dirac points. The gaps at $(-K, 0)$ point change in an opposite way with θ . These points are identically gapped for $\theta = \pi/2$.

2. Brillouin-Wigner evaluation of the Floquet Hamiltonian

We now formulate the high frequency effective Hamiltonian which enables us to study the phase diagram of Chern numbers in the various parameter space. To this end, we employ the Brillouin-Wigner (BW) perturbation theory to construct the high frequency effective Hamiltonian on the projected zero-photon subspace of Floquet theory⁷³. This correctly reproduces the quasienergies and the eigenstates associated with the original Floquet Hamiltonian up to order $1/\omega$. Specifically, a projector operator projects the whole Hilbert space $H \otimes T$ onto the zero photon subspace $H \otimes T_0 \sim H$. On the other hand, the wave-operator restores the eigenstates of $H \otimes T$ from the projected space of $H \otimes T_0$. The effective Hamiltonian is then expressed in terms of this wave operator that can be determined in powers of $1/\omega$ recursively. This theory has a number of advantages over the other high frequency

perturbation theories namely, i.e the Floquet-Magnus expansion and van Vleck expansion, being that the BW theory rectifies the driving phase dependence problem appearing in the Floquet-Magnus expansion. Additionally, BW theory can be used to get the higher order terms which are challenging to compute using the van Vleck theory.

Having stated the BW theory in a nutshell, we revert to the associated final effective Hamiltonian $H_{\text{BW}} = \sum_{n=0}^{\infty} H_{\text{BW}}^{(n)}$ with

$$H_{\text{BW}}^{(0)} = H_{0,0}, \quad H_{\text{BW}}^{(1)} = \sum_{\{n_i\} \neq 0} \frac{H_{0,n_1} H_{n_1,0}}{n_1 \omega}$$

and

$$H_{\text{BW}}^{(2)} = \sum_{\{n_i\} \neq 0} \left(\frac{H_{0,n_1} H_{n_1,n_2} H_{n_2,0}}{n_1 n_2 \omega^2} - \frac{H_{0,n_1} H_{n_1,0} H_{0,0}}{n_1^2 \omega^2} \right).$$

In the process of quantifying each term $H_{m,n}$ in the above expression, we need to compute the hopping strength accordingly in the presence of the laser fields⁷³. The hopping strength from A sub lattice to B sub lattice becomes $t_{AB}^{n,l} = \sum_m J_{-n-2m}(-A_R) J_m(A_L) e^{-im\theta} e^{\frac{i2\pi l(3m+n)}{3}}$. Similarly, the $B-A$ hopping is given by $t_{BA}^{n,l} = \sum_m J_{-n-2m}(A_R) J_m(-A_L) e^{-im\theta} e^{\frac{i2\pi l(3m+n)}{3}}$. While doing the calculation of the perturbation theory term by term, a variety of new hopping terms gets generated. Below shall explicitly mention them.

We now explicitly write the NN hopping J_1 obtained from $H_{\text{BW}}^{(0)}$, $H_{\text{BW}}^{(2)}$ terms

$$\begin{aligned} a_i^\dagger b_{i+p} : J_1 = & t_{AB}^{0,p} + \sum_{n \neq 0} \frac{-1}{n^2 \omega^2} \left(\sum_{q=0,1,2} t_{AB}^{-n,p} t_{BA}^{n,q} t_{AB}^{q,0} \sum_{q \neq p}^{q=0,1,2} t_{AB}^{-n,q} t_{BA}^{n,q} t_{AB}^{0,p} \right) \\ & + \sum_{n,m \neq 0} \frac{1}{mn \omega^2} \left(\sum_{q=0,1,2} t_{AB}^{-n,p} t_{BA}^{n-m,q} t_{AB}^{m,q} + \sum_{q=0,1,2}^{q \neq p} t_{AB}^{-n,q} t_{BA}^{n-m,q} t_{AB}^{m,p} \right) \end{aligned} \quad (\text{C1})$$

where p represents the links $l = 0, 1, 2$ for NN hopping. Now, NNN terms J_2 , obtained from $H_{\text{BW}}^{(1)}$, are given by

$$a_i^\dagger a_{i+p-q} : J_2^A = \sum_{n \neq 0} \frac{-1}{n\omega} t_{AB}^{-n,p} t_{BA}^{n,q} \quad (\text{C2})$$

$$b_i^\dagger b_{i+p-q} : J_2^B = \sum_{n \neq 0} \frac{-1}{n\omega} t_{BA}^{-n,p} t_{AB}^{n,q}. \quad (\text{C3})$$

The mass terms m_A and m_B can be obtained from the above expressions of $a_i^\dagger a_{i+p-q}$ and $b_i^\dagger b_{i+p-q}$ with $p = q$. The third nearest neighbour hopping connected by M -

links⁷³ J_3 , obtained from $H_{\text{BW}}^{(2)}$, are given by

$$\begin{aligned} a_i^\dagger b_{i+2p-q} : J_3 = & \sum_{n \neq 0} \frac{-1}{n^2 \omega^2} [t_{AB}^{-n,p} t_{BA}^{n,q} t_{AB}^{0,p}] \\ & + \sum_{n,m \neq 0} \frac{1}{nm \omega^2} t_{AB}^{-n,p} t_{BA}^{n-m,q} t_{AB}^{m,p}, \end{aligned} \quad (\text{C4})$$

where $p \neq q = 0, 1, 2$. The other type of third nearest neighbour hopping connected by L -links J_4 ⁷³, obtained

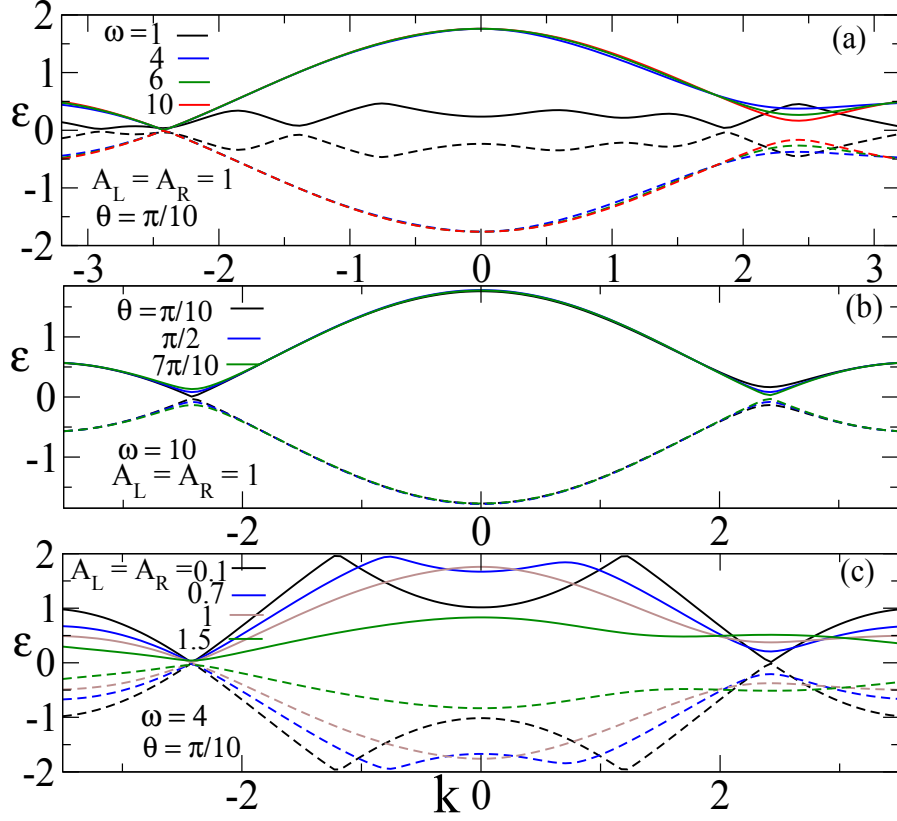


FIG. 7. Variation of quasi-energy ϵ with k_x keeping $k_y = 0$ for different values of frequency (a), relative phase (b), and amplitude (c). (a): The gap at $(-K, 0)$ is much smaller than that of the at $(K, 0)$. This asymmetry of gaps is reduced as one increases ω i.e., the gap appearing at $(K, 0)$ decreases, whereas, the other one changes insignificantly. The gap also increases in the central part with ω within the same temporal BZ. (b): Gap at $(-K, 0)$ increases with increasing θ within the range $0 < \theta < \pi$, while gap at $(K, 0)$ decreases. For $\theta = \pi/2$ both of them become symmetrically gapped. (c): Both the Dirac points are insignificantly gapped for smaller amplitude; the gap at $(K, 0)$ increases with A_L . Although, for smaller amplitude the gaps between two consecutive photon sector appear symmetrically around $k_x = 0$; they disappear for higher amplitudes.

from $H_{BW}^{(2)}$, are given by

$$a_i^\dagger b_{i+p-q+r} : J_A = \sum_{n \neq 0} \frac{-1}{n^2 \omega^2} [t_{AB}^{-n,p} t_{BA}^{n,q} t_{AB}^{0,r}] + \sum_{n,m \neq 0} \frac{1}{nm \omega^2} t_{AB}^{-n,p} t_{BA}^{n-m,q} t_{AB}^{m,r}, \quad (C5)$$

with $p \neq q \neq r = 0, 1, 2$. The hermitian conjugate of the above terms (Eq.(C1), (C4), (C5)) gives the hopping from B sub lattice to A sub lattice; in this case t_{AB} is replaced by t_{BA} and vice versa. The final Hamiltonian

looks like

$$H_{BW} = \sum_{i,p}^{NN} J_1 a_i^\dagger b_{i+p} + \sum_{i,p \neq q}^{NNN, A(B)} J_2^{A(B)} a(b)_i^\dagger a(b)_{i+p-q} + \sum_{i,p \neq q \neq r}^{L-links} J_4 a_i^\dagger b_{i+p-q+r} + \sum_{i,p \neq q}^{M-links} J_3 a_i^\dagger b_{i+2p-q} + h.c. + \sum_i^{A(B)-sublattice} m_{A(B)} a(b)_i^\dagger a(b)_i + h.c. \quad (C6)$$

Hence, the high frequency expansion gives rise to a momentum independent mass term that breaks the inversion symmetry. This is the reason why CDW order oscillates with real time inside the switch OFF region. Having formulated the Hamiltonian in real space, one can go to Fourier space where H_{BW} is decomposed in different momentum segments, $H_{BW} = \prod_k H_{BW}^k$. The mass terms associated with σ_z is responsible for opening up a gap in the spectrum which eventually leads to non-trivial topo-

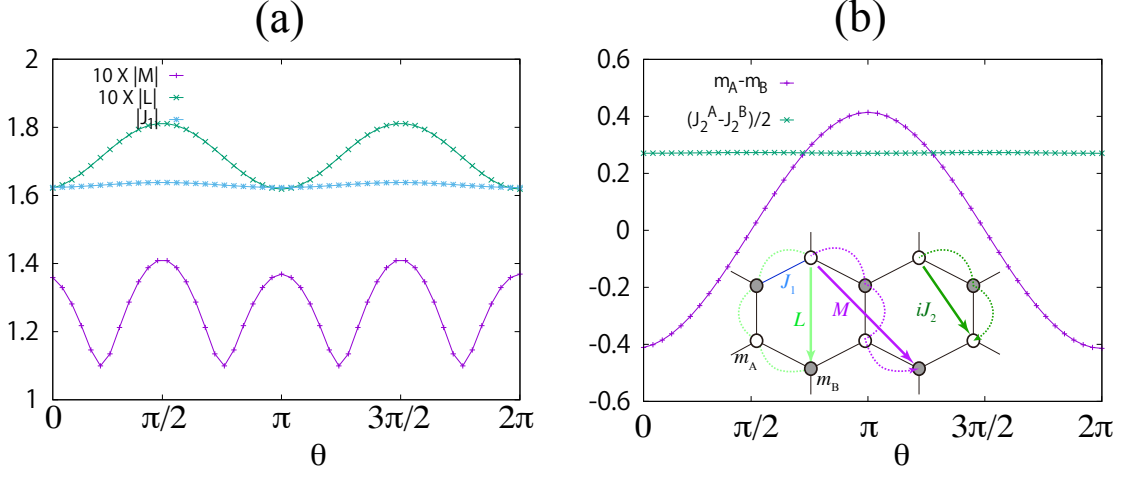


FIG. 8. (a) The plot shows the variation of the magnitude of the off-diagonal hopping terms with θ . As expected, $|J_1|$ is most significant contributor and $|M|$ contributes insignificantly. The common fact is that $|J_1|$ and $|L|$ both exhibits a maxima near $\theta = \pi/2$ and a minima at $\theta = \pi$. While $|M|$ shows local maxima at $\theta = \pi/2, \pi$ and minima at $\theta = 3\pi/4$. (b) The plot shows the diagonal mass terms and the hopping term to same sub-lattice as a function of θ . Interestingly, $m_A - m_B$ changes its sign when $\theta = \pi/2$. Inset depicts the geometrical description of different terms.

logical phases.

One can think of H_{BW}^k as a spin Hamiltonian with \mathbf{k} dependent magnetic field terms i.e., $H_{BW}^k = \mu B_{\mathbf{k}} \cdot \sigma$. Since the 2×2 , momentum space effective Hamiltonian consists of the different kinds of hopping terms e.g., nearest neighbour hopping J_1 , long range hopping J_2, J_3 and J_4 and on-site terms $m_{A(B)}$. Among these terms J_2 represents the hopping between the same sub-lattice. Therefore, the diagonal terms are given by momentum independent mass terms along with the momentum dependent $J_2 \cos(\mathbf{k}(p-q))$. On the other hand, the off-diagonal terms are given by $J_1 \exp(\pm i\mathbf{k}p)$, $J_3 \exp(\pm i\mathbf{k}(2p-q))$ and $J_4 \exp(\pm i\mathbf{k}(p-q+r))$. Therefore, the explicit momentum dependent magnetic fields are $B_{kx} = J_1 \cos(\mathbf{k}p) + J_3 \cos(\mathbf{k}(2p-q)) + J_4 \cos(\mathbf{k}(p-q+r))$, $B_{ky} = J_1 \sin(\mathbf{k}p) + J_3 \sin(\mathbf{k}(2p-q)) + J_4 \sin(\mathbf{k}(p-q+r))$, $B_{kz} = J_2 \cos(\mathbf{k}(p-q)) + (m_A - m_B)$. In order to clearly investigate the effect of each terms, we study the momentum independent coefficients namely, J_1, J_2, J_3, J_4 , and $m_A - m_B$ as a function of θ . This would provide a clear connection to the spin echo analogy for $\theta = \pi/2$ as discussed in the main text.

Figure 8 shows the behavior of the effective terms while θ is varied. Since J_1 represents the nearest neighbour hopping, its magnitude becomes largest among the hoppings. The M -link hopping refers to the maximum long range hopping amplitude and hence its magnitude is the smallest. While L -link hopping are intermediate range. The interesting common fact about all the above hopping is that they all show oscillatory behavior with θ and acquire maximum magnitude at $\theta = \pi/2, 3\pi/2$. On the other hand, the NN-link hopping and L -link hopping both acquires minimum magnitude at $\theta = 0$. The

M -links hopping becomes minimum for $\theta = \pi/4, 3\pi/4, 5\pi/4$ and $7\pi/4$. It again shows a secondary maxima at $\theta = 0, \pi$ and 2π . On the other hand, for diagonal mass term $m_A - m_B$ changes its sign at $\theta = \pi/2$ and $3\pi/2$. It becomes maximally negative and positive at $\theta = 0$ and π . Therefore, it can be inferred that $\theta = 0$ and π refers to the two extreme situation where CDW order acquires its maximum magnitude and the off-diagonal terms become insignificant. On the other hand, for $\theta = \pi/2$ and $3\pi/2$, the mass term becomes zero and gives room for the other terms to significantly alter the dynamics of the CDW order.

Relating the above finding to the spin echo technique, employed in NMR, one can say that z -component magnetization is caused by B_{kz} . When the ‘‘transverse fields’’ B_{kx}, B_{ky} acquire maximum values, the magnetization along z -direction can get flipped. This is due to fact that $\sigma_{x,y}$ does not commute with σ_z and hence this off-diagonal term results in a precession. We note that the above argument is based on the Floquet effective Hamiltonian in the non-interacting case. For the interacting case, this argument is not guaranteed to hold. However, from our numerical findings, it still provides a qualitative understanding for the flipping of CDW order as displayed in Fig. 1e (main text).

Appendix D: Time glide symmetry, topology and Road to self-maintained Floquet crystalline states

We now investigate the emergence of edge state in a minimal model, considered for the switch off region, with an open boundary condition in x -direction. Existence

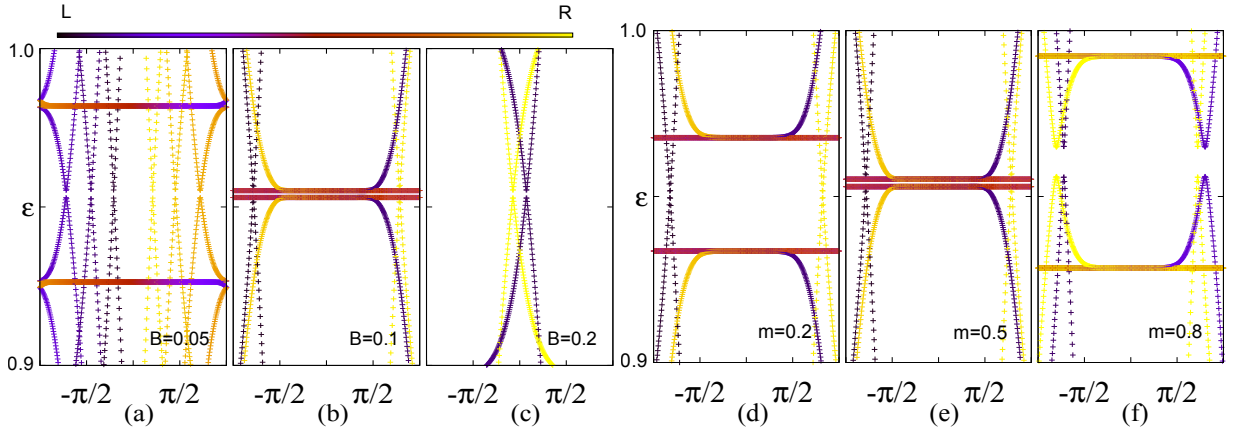


FIG. 9. Quasi-energy dispersion of the Floquet Hamiltonian as function of k_y for various parameter values. The colour map indicates the weight of states on each lattice sites. The first three panels show that increasing B leads to a topological phase transition between two distinct topological phase by a closing of the bulk gap; here m is kept at 0.5. (a) Topological phase with three pairs of edge state. (b) Closing of the bulk band gap due to the vanishing the gaps between of the flat bulk modes. (c) Another topological phase emergences with one pair of edge state. The last three panels show the transition from a topological phase to a non-topological phase by varying m keeping $B = 0.1$. (d) A situation where only 1 pair of edge state appear between the bulk flat band. (e) Bulk gap closing. (f) Non-topological phase having no π edge states. In all case the lattice size $N = 200$.

of such edge states that persist and appear upon band gap closings, directly conveys the topological nature of the model in certain parameter regimes. This indicates the potential of DST setups to create novel Floquet crystalline states that are protected by space-time symmetries.

In the OFF region, when DST takes place, an oscillating CDW order is formed. Let us investigate this situation using a simplified lattice model

$$H(t) = H_0 + \lambda \Delta(t) \sum_i (c_{A_i}^\dagger c_{A_i} - c_{B_i}^\dagger c_{B_i}) \quad (D1)$$

where H_0 denotes the non-interacting tight binding model for electrons on the honeycomb lattice as given in Eq. (2) in the main text, and $\Delta(t) = m \sin(\Omega_0 t)$ represents the CDW order oscillation and $\Omega_0 = 1.9$ is the system selected frequency. Importantly, this model has a chiral symmetry: $\Gamma \mathcal{H}_{\mathbf{k}}(t) \Gamma = -\mathcal{H}_{\mathbf{k}}(-t)$ in the momentum space picture with $\mathcal{H}_{\mathbf{k}}(t) = \Delta(t) \sigma_z + h_x \sigma_x + h_y \sigma_y$ and $\Gamma = \sigma_z$. The corresponding real space model has a time glide symmetry as alluded in the main text, $H(t) = M H(t + T/2) M^{-1}$ ($T = 2\pi/\Omega_0$) where M is the mirror symmetry that is broken by the AB-sublattice potential. The Floquet topological crystalline states protected by the time glide symmetry can now directly be investigated by checking whether the system supports π chiral edge states. Their existence is also closely tied to the chiral symmetry and have been proposed in theoretical models before⁴⁶. In order to look for edge states, we consider an extra static magnetic field $B = (0, 0, B)$. This will modify the hopping through a phase factor $\exp(i \int A \cdot dr)$ with vector potential $A = (0, Bx, 0)$. Given this model, we consider an armchair edge in the brick wall lattice geometry. We diagonalize the Floquet Hamilto-

nian to obtain the quasi-energy, quasi-states and the associated average weight of each state on the lattice sites.

The results plotted in Fig. (9) show that, depending on the parameter regions, π edge mode indeed appear. The π edge modes are states spatially localised at the edge of the system appearing at $\varepsilon = \pm \Omega_0/2$ in the Floquet quasi-energy space, and characterise dynamically extended topology of periodically driven systems²¹. We also find several topological transitions when the bulk gap vanishes and reopens. The left three panels of Fig. (9) convey that there is a topological transition between two topological phases as the field strength is increased as the gap close and reopens at $B = 0.1$ while the strength of the CDW oscillation m is kept fixed to $m = 0.5$. We also remark that the topological phases are always characterised by an even number of edges modes i.e., edge states appear always in pairs. For example, Fig. (9a) depicts a situation where three pairs of modes appear at quasi-energy $\varepsilon = \Omega_0/2$ at the left boundary and another three pairs of modes at the right boundary; each pair consists of two opposite chirality. Moreover, it is noteworthy that bulk bands close to $\varepsilon = \Omega_0/2$ becomes flat and the band gap vanishes at the topological transition point. One can also vary m to encounter a topological phase transition as observed in Fig. (9e) with $B = 0.1$. In the right three panels of Fig. (9), we exemplify a situation where a topological phase is separated from a non-topological phase by a bulk gap closing. The non-topological phase does not contain any edge state at $\varepsilon = \Omega_0/2$. This asserts that topological phases protected by Floquet crystalline symmetries can indeed be induced by the DST setup.

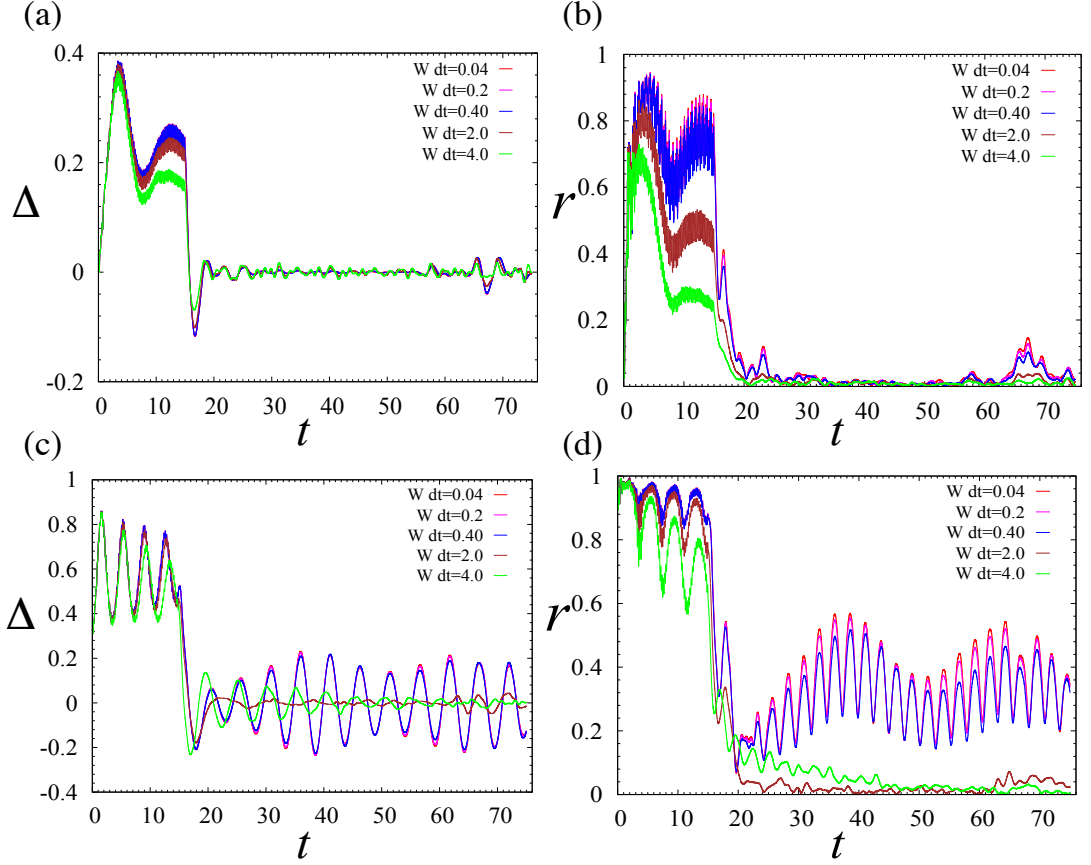


FIG. 10. The time evolution of Δ and r are shown for $V = 0.3$ in (a) and (b), respectively. The same for $V = 0.8$ are shown in (c) and (d). Here, we consider graphene model (i) with momentum-time dependent random mass term. The strength of this disorder is given by Wdt . The synchronization is substantially affected by the disorder as observed for $V = 0.8$. Here, $\omega = 10$ and $\theta = \pi/10$.

Appendix E: Going beyond mean field

We did not consider heating in our calculation. It has been a central topic of interest to study the heating effect in a periodically driven system. Recent studies in the context of many body systems show that prethermalization takes place in the high-frequency regime^{59,60,74}. What is argued there is that for a finite time window, the dynamics of an interacting system can be described within the Floquet effective Hamiltonian approach⁷⁴. In our problem, the pulse duration of the laser field is finite and can be made short to fit within the Floquet prethermalization window.

We note that when the pulse duration becomes exponentially long, then the system would not be restricted inside the prethermal regime. Once the system starts absorbing energy, there would be substantial reduction of the synchronization. Hence the synchronization order parameter r is expected to decrease. Similarly, in the switch off regime, r would decrease. In order to clarify the heating effect arising from scattering, we perform an

additional numerical calculation below.

In the mean field approximation no scattering process are considered. However, in order to accommodate the effect of relaxation due to electron-electron or electron-phonon scatterings, we extend the mean field treatment by considering a random mass term in the momentum space which changes its value for each momentum and time instant $M = \eta(t, k)$ with η chosen from a Gaussian distribution centered around zero. This term mimics the effect of a Hubbard-Stratonovich field that arises when an electron-electron interaction is incorporated⁷⁵. The dynamical evolution of CDW order Δ and the synchronization order parameter r are shown in Fig. 10. For low disorder strength, r is quantitatively unaltered in the both switch off and on region. The CDW order behaves similarly as $M = 0$. For substantial disorder strength, r decreases in the switch on region. While in the switch OFF region, r decreases to zero within a window of time after the switch on region. This window of time gradually decreases with increasing disorder strength. Therefore, the long time average value of r , r_{av} becomes zero

when the disorder is substantial. This refers to the fact that the synchronization transition would disappear for strong disorder.

Now, we shall elaborate the above discussion. The interesting observation in the OFF region is that for substantial disorder strength $Wdt > 0.4$, CDW order Δ continues to show coherent oscillation in a short window of time $15 < t < 40$ (see Fig. 10 c). Inside this temporal regime, r also remains finite, signifying the fact that system remain in the synchronized phase (see Fig. 10 d). As time passes by $t > 40$, Δ starts dephasing and continues aperiodic random oscillation for further time. There, synchronization order parameter r decreases and becomes small. Hence, under a sufficiently long relaxation time, we expect that r_{av} as well as the oscillation amplitude in Δ diminish to zero. The time duration for which the coherence is remained is a few hundred time periods:

$\delta t = 2m\pi/\omega$, with $m \sim O(10^2)$. The higher strength of the disorder is equivalent to a higher degree of momentum mixing due to the electron-electron scattering. For relatively small interaction strength $V = 0.3$, when graphene remains in a non-synchronized phase with the same driving frequency, the temporal window δt becomes vanishingly small, as expected (see Fig. 10 a, b).

We can now make some general comment regarding the scattering phenomena. We know from the existing literature that relaxation time in graphene is large compared to the strongly correlated cuprates where it is femtosecond. Experimentally, it has been shown that relaxation time in graphene is of the order of picoseconds⁵⁸. Additionally, in low temperature, the phonon scattering is reduced. Hence, we think that even in the presence of scattering, a few cycles of coherent oscillation in Δ can be observed after switching off the laser field.

-
- ¹ Iwai, S. & Okamoto, H. Ultrafast phase control in one-dimensional correlated electron systems. *Journal of the Physical Society of Japan* **75**, 011007–011007 (2006).
- ² Basov, D. N., Averitt, R. D., van der Marel, D., Dressel, M. & Haule, K. Electrodynamics of correlated electron materials. *Rev. Mod. Phys.* **83**, 471–541 (2011). URL <https://link.aps.org/doi/10.1103/RevModPhys.83.471>.
- ³ Yonemitsu, K. & Nasu, K. Theory of photoinduced phase transitions in itinerant electron systems. *Physics Reports* **465**, 1 – 60 (2008). URL <http://www.sciencedirect.com/science/article/pii/S0370157308001476>.
- ⁴ Aoki, H. *et al.* Nonequilibrium dynamical mean-field theory and its applications. *Reviews of Modern Physics* **86**, 779–837 (2014). URL <http://link.aps.org/doi/10.1103/RevModPhys.86.779>.
- ⁵ Giannetti, C. *et al.* Ultrafast optical spectroscopy of strongly correlated materials and high-temperature superconductors: a non-equilibrium approach. *Advances in Physics* **65**, 58–238 (2016).
- ⁶ Cavalleri, A. *et al.* Femtosecond structural dynamics in vo_2 during an ultrafast solid-solid phase transition. *Phys. Rev. Lett.* **87**, 237401 (2001). URL <https://link.aps.org/doi/10.1103/PhysRevLett.87.237401>.
- ⁷ Iwai, S. *et al.* Ultrafast optical switching to a metallic state by photoinduced mott transition in a halogen-bridged nickel-chain compound. *Phys. Rev. Lett.* **91**, 057401 (2003). URL <https://link.aps.org/doi/10.1103/PhysRevLett.91.057401>.
- ⁸ Perfetti, L. *et al.* Time evolution of the electronic structure of $1t\text{-tas}_2$ through the insulator-metal transition. *Phys. Rev. Lett.* **97**, 067402 (2006). URL <https://link.aps.org/doi/10.1103/PhysRevLett.97.067402>.
- ⁹ Kaiser, S. *et al.* Optically induced coherent transport far above T_c in underdoped $\text{yba}_2\text{cu}_3\text{o}_{6+\delta}$. *Phys. Rev. B* **89**, 184516 (2014). URL <https://link.aps.org/doi/10.1103/PhysRevB.89.184516>.
- ¹⁰ Hu, W. *et al.* Optically enhanced coherent transport in $\text{yba}_2\text{cu}_3\text{o}_{6.5}$ by ultrafast redistribution of interlayer coupling. *Nature Materials* **13**, 705 EP – (2014). URL <http://dx.doi.org/10.1038/nmat3963>.
- ¹¹ Mankowsky, R. *et al.* Nonlinear lattice dynamics as a basis for enhanced superconductivity in $\text{yba}_2\text{cu}_3\text{o}_{6.5}$. *Nature* **516**, 71 EP – (2014). URL <http://dx.doi.org/10.1038/nature13875>.
- ¹² Nova, T. F. *et al.* An effective magnetic field from optically driven phonons. *Nature Physics* **13**, 132 EP – (2016). URL <http://dx.doi.org/10.1038/nphys3925>.
- ¹³ Foster, M. S., Dzero, M., Gurarie, V. & Yuzbashyan, E. A. Quantum quench in a $p + ip$ superfluid: Winding numbers and topological states far from equilibrium. *Phys. Rev. B* **88**, 104511 (2013). URL <https://link.aps.org/doi/10.1103/PhysRevB.88.104511>.
- ¹⁴ Foster, M. S., Gurarie, V., Dzero, M. & Yuzbashyan, E. A. Quench-induced floquet topological p -wave superfluids. *Phys. Rev. Lett.* **113**, 076403 (2014). URL <https://link.aps.org/doi/10.1103/PhysRevLett.113.076403>.
- ¹⁵ Eckardt, A. Colloquium: Atomic quantum gases in periodically driven optical lattices. *Reviews of Modern Physics* **89**, 1–30 (2017). 1606.08041.
- ¹⁶ Oka, T. & Kitamura, S. Floquet Engineering of Quantum Materials 1804.03212.
- ¹⁷ Oka, T. & Aoki, H. Photovoltaic hall effect in graphene. *Phys. Rev. B* **79**, 081406 (2009). URL <https://link.aps.org/doi/10.1103/PhysRevB.79.081406>.
- ¹⁸ Lindner, N. H., Refael, G. & Galitski, V. Floquet topological insulator in semiconductor quantum wells. *Nature Physics* **7**, 490 EP – (2011). URL <http://dx.doi.org/10.1038/nphys1926>.
- ¹⁹ Kitagawa, T., Berg, E., Rudner, M. & Demler, E. Topological characterization of periodically driven quantum systems. *Phys. Rev. B* **82**, 235114 (2010). URL <https://link.aps.org/doi/10.1103/PhysRevB.82.235114>.
- ²⁰ Jiang, L. *et al.* Majorana fermions in equilibrium and in driven cold-atom quantum wires. *Phys. Rev. Lett.* **106**, 220402 (2011). URL <https://link.aps.org/doi/10.1103/PhysRevLett.106.220402>.
- ²¹ Rudner, M. S., Lindner, N. H., Berg, E. & Levin, M. Anomalous edge states and the bulk-edge correspondence for periodically driven two-dimensional systems. *Phys. Rev. X* **3**, 031005 (2013). URL <https://link.aps.org/doi/10.1103/PhysRevX.3.031005>.
- ²² Wang, Y. H., Steinberg, H., Jarillo-Herrero, P. &

- Gedik, N. Observation of Floquet-Bloch States on the Surface of a Topological Insulator. *Science* **342**, 453–457 (2013). URL <http://www.sciencemag.org/cgi/doi/10.1126/science.1239834><http://www.sciencemag.org/content/342/6157/453.short>.
- ²³ Jotzu, G. *et al.* Experimental realization of the topological Haldane model with ultracold fermions. *Nature* **515**, 237–240 (2014). URL <http://dx.doi.org/10.1038/nature13915><http://www.nature.com/nature/journal/v515/n7526/abs/nature13915.html#supplementary-information>.
- ²⁴ Rechtsman, M. C. *et al.* Photonic floquet topological insulators. *Nature* **496**, 196 EP – (2013). URL <http://dx.doi.org/10.1038/nature12066>.
- ²⁵ Kinoshita, S., Murata, K. & Oka, T. Holographic floquet states ii: Floquet condensation of vector mesons in nonequilibrium phase diagram. *Journal of High Energy Physics* **2018**, 96 (2018). URL [https://doi.org/10.1007/JHEP06\(2018\)096](https://doi.org/10.1007/JHEP06(2018)096).
- ²⁶ Littlewood, P. B. & Varma, C. M. *Phys. Rev. Lett.* **47**, 811 (1981).
- ²⁷ Littlewood, P. B. & Varma, C. M. *Phys. Rev. B* **26**, 4883 (1982).
- ²⁸ Matsunaga, R., Matsuda, K. & Kanemitsu, Y. Observation of Charged Excitons in Hole-Doped Carbon Nanotubes Using Photoluminescence and Absorption Spectroscopy. *Physical Review Letters* **106**, 1–4 (2011). URL <http://link.aps.org/doi/10.1103/PhysRevLett.106.037404>.
- ²⁹ Matsunaga, R. *et al.* Light-induced collective pseudospin precession resonating with Higgs mode in a superconductor. *Science (New York, N.Y.)* **1145**, 1–7 (2014). URL <http://www.ncbi.nlm.nih.gov/pubmed/25011555>.
- ³⁰ Tsang, J. C., Smith, J. J. E. & M Shafer, M. W. *Phys. Rev. Lett.* **37**, 1407 (1976).
- ³¹ J. Demsar, J., Biljakovic, K. & Mihailovic, D. *Phys. Rev. Lett.* **83**, 800 (1999).
- ³² Pekker, D. & Varma, C. Amplitude/higgs modes in condensed matter physics. *Annual Review of Condensed Matter Physics* **6**, 269–297 (2015).
- ³³ Castro Neto, A. H., Guinea, F., Peres, N. M. R., Novoselov, K. S. & Geim, A. K. The electronic properties of graphene. *Rev. Mod. Phys.* **81**, 109–162 (2009). URL <https://link.aps.org/doi/10.1103/RevModPhys.81.109>.
- ³⁴ Brumer, P. & Shapiro, M. Control of unimolecular reactions using coherent light. *Chemical Physics Letters* **126**, 541 – 546 (1986). URL <http://www.sciencedirect.com/science/article/pii/S0009261486801713>.
- ³⁵ Ishikawa, K. L. Nonlinear optical response of graphene in time domain. *Phys. Rev. B* **82**, 201402 (2010). URL <https://link.aps.org/doi/10.1103/PhysRevB.82.201402>.
- ³⁶ Rioux, J., Burkard, G. & Sipe, J. E. Current injection by coherent one- and two-photon excitation in graphene and its bilayer. *Phys. Rev. B* **83**, 195406 (2011). URL <https://link.aps.org/doi/10.1103/PhysRevB.83.195406>.
- ³⁷ Keldar, H. K., Apalkov, V. & Stockman, M. I. Graphene in ultrafast and superstrong laser fields. *Phys. Rev. B* **91**, 045439 (2015). URL <https://link.aps.org/doi/10.1103/PhysRevB.91.045439>.
- ³⁸ Higuchi, T., Heide, C., Ullmann, K., Weber, H. B. & Hommelhoff, P. Light-field-driven currents in graphene. *Nature* **550**, 224 EP – (2017). URL <http://dx.doi.org/10.1038/nature23900>.
- ³⁹ Kfir, O. *et al.* Generation of bright phase-matched circularly-polarized extreme ultraviolet high harmonics. *Nature Photonics* **9**, 99 EP –.
- ⁴⁰ Wehling, T. O. *et al.* Strength of effective coulomb interactions in graphene and graphite. *Phys. Rev. Lett.* **106**, 236805 (2011). URL <https://link.aps.org/doi/10.1103/PhysRevLett.106.236805>.
- ⁴¹ Oka, T. Nonlinear doublon production in a mott insulator: Landau-dykhne method applied to an integrable model. *Phys. Rev. B* **86**, 075148 (2012). URL <https://link.aps.org/doi/10.1103/PhysRevB.86.075148>.
- ⁴² Kuramoto, Y. *Chemical Oscillations, Waves, and Turbulence* (Springer-Verlag Berlin, Heidelberg, 1984).
- ⁴³ Acebrón, J. A., Bonilla, L. L., Pérez Vicente, C. J., Ritort, F. & Spigler, R. The kuramoto model: A simple paradigm for synchronization phenomena. *Rev. Mod. Phys.* **77**, 137–185 (2005). URL <https://link.aps.org/doi/10.1103/RevModPhys.77.137>.
- ⁴⁴ Yoshikawa, N., Tamaya, T. & Tanaka, K. High-harmonic generation in graphene enhanced by elliptically polarized light excitation. *Science* **356**, 736–738 (2017).
- ⁴⁵ Mak, K. F., Shan, J. & Heinz, T. F. Seeing many-body effects in single- and few-layer graphene: Observation of two-dimensional saddle-point excitons. *Phys. Rev. Lett.* **106**, 046401 (2011). URL <http://link.aps.org/doi/10.1103/PhysRevLett.106.046401>.
- ⁴⁶ Morimoto, T., Po, H. C. & Vishwanath, A. Floquet topological phases protected by time glide symmetry. *Phys. Rev. B* **95**, 195155 (2017). URL <https://link.aps.org/doi/10.1103/PhysRevB.95.195155>.
- ⁴⁷ Qi, X.-L. & Zhang, S.-C. Topological insulators and superconductors. *Rev. Mod. Phys.* **83**, 1057–1110 (2011). URL <https://link.aps.org/doi/10.1103/RevModPhys.83.1057>.
- ⁴⁸ Hasan, M. Z. & Kane, C. L. Colloquium. *Rev. Mod. Phys.* **82**, 3045–3067 (2010). URL <https://link.aps.org/doi/10.1103/RevModPhys.82.3045>.
- ⁴⁹ Fu, L. Topological crystalline insulators. *Phys. Rev. Lett.* **106**, 106802 (2011). URL <https://link.aps.org/doi/10.1103/PhysRevLett.106.106802>.
- ⁵⁰ Slager, R.-J., Mesaros, A., Juričić, V. & Zaenen, J. The space group classification of topological band-insulators. *Nature Physics* **9**, 98 (2012). URL <http://dx.doi.org/10.1038/nphys2513>.
- ⁵¹ Kruthoff, J., de Boer, J., van Wezel, J., Kane, C. L. & Slager, R.-J. Topological classification of crystalline insulators through band structure combinatorics. *Phys. Rev. X* **7**, 041069 (2017). URL <https://link.aps.org/doi/10.1103/PhysRevX.7.041069>.
- ⁵² Po, H. C., Vishwanath, A. & Watanabe, H. Symmetry-based indicators of band topology in the 230 space groups. *Nature Communications* **8**, 50 (2017). URL <https://doi.org/10.1038/s41467-017-00133-2>.
- ⁵³ Bradlyn, B. *et al.* Topological quantum chemistry. *Nature* **547**, 298 (2017). URL <http://dx.doi.org/10.1038/nature23268>.
- ⁵⁴ Xu, S. & Wu, C. Space-time crystal and space-time group. *Phys. Rev. Lett.* **120**, 096401 (2018). URL <https://link.aps.org/doi/10.1103/PhysRevLett.120.096401>.
- ⁵⁵ Nag, T., Slager, R.-J., Higuchi, T. & Oka, T. *In preparation*.
- ⁵⁶ Slager, R.-J. The translational side of topological band insulators (2017). ArXiv:1708.08886.
- ⁵⁷ Slager, R.-J., Mesaros, A., Juričić, V. & Zaenen, J. Interplay between electronic topology and crystal symme-

- try: Dislocation-line modes in topological band insulators. *Phys. Rev. B* **90**, 241403 (2014). URL <https://link.aps.org/doi/10.1103/PhysRevB.90.241403>.
- ⁵⁸ Gierz, I. *et al.* Snapshots of non-equilibrium Dirac carrier distributions in graphene. *Nature Materials* **12**, 1119 EP –.
- ⁵⁹ Abanin, D. A., De Roeck, W., Ho, W. W. & Huvener, F. m. c. Effective hamiltonians, prethermalization, and slow energy absorption in periodically driven many-body systems. *Phys. Rev. B* **95**, 014112 (2017). URL <https://link.aps.org/doi/10.1103/PhysRevB.95.014112>.
- ⁶⁰ Weidinger, S. A. & Knap, M. Floquet prethermalization and regimes of heating in a periodically driven, interacting quantum system. *Scientific Reports* **7**, 45382 EP –.
- ⁶¹ Barankov, R. A., Levitov, L. S. & Spivak, B. Z. Solitons and rabi oscillations in a time-dependent bcs pairing problem. *Phys. Rev. Lett.* **93**, 1640401 (2004).
- ⁶² Kuramoto, Y. in *International Symposium on Mathematical Problems in Theoretical Physics edited by H. Araki, (Springer, New York, 1975)* .
- ⁶³ Kuramoto, Y. *Chemical Oscillations, Waves and Turbulence (Springer, New York, 1984)* .
- ⁶⁴ Strogatz, S. H., Marcus, C. M., Westervelt, R. M. & Mirolo, R. E. Simple model of collective transport with phase slippage. *Phys. Rev. Lett.* **61**, 2380–2383 (1988). URL <https://link.aps.org/doi/10.1103/PhysRevLett.61.2380>.
- ⁶⁵ Acebrón, J. A., Bonilla, L. L., Pérez Vicente, C. J., Ritort, F. & Spigler, R. The kuramoto model: A simple paradigm for synchronization phenomena. *Rev. Mod. Phys.* **77**, 137–185 (2005). URL <https://link.aps.org/doi/10.1103/RevModPhys.77.137>.
- ⁶⁶ Rodrigues, F. A., Peron, T. K. D., Ji, P. & Kurths, J. The kuramoto model in complex networks. *Physics Reports* **610**, 1 – 98 (2016). URL <http://www.sciencedirect.com/science/article/pii/S0370157315004408>. The Kuramoto model in complex networks.
- ⁶⁷ Maistrenko, Y., Popovych, O., Burylko, O. & Tass, P. A. Mechanism of desynchronization in the finite-dimensional kuramoto model. *Phys. Rev. Lett.* **93**, 084102 (2004). URL <https://link.aps.org/doi/10.1103/PhysRevLett.93.084102>.
- ⁶⁸ Maistrenko, V., Vasylenko, A., Maistrenko, Y. & Mosekilde, E. Phase chaos and multistability in the discrete kuramoto model. *Nonlinear Oscillations* **11**, 229–241 (2008). URL <https://doi.org/10.1007/s11072-008-0026-4>.
- ⁶⁹ Childs, L. M. & Strogatz, S. H. Stability diagram for the forced kuramoto model. *Chaos: An Interdisciplinary Journal of Nonlinear Science* **18**, 043128 (2008). URL <https://doi.org/10.1063/1.3049136>. <https://doi.org/10.1063/1.3049136>.
- ⁷⁰ Shirley, J. *Phys. Rev.* **138**, B979 (1965).
- ⁷¹ Griffoni, M. & Hanggi, P. *Physics Reports* **304**, 229 (1998).
- ⁷² Kitagawa, T., Oka, T., Brataas, A., Fu, L. & Demler, E. Transport properties of nonequilibrium systems under the application of light: Photoinduced quantum hall insulators without landau levels. *Phys. Rev. B* **84**, 235108 (2011). URL <https://link.aps.org/doi/10.1103/PhysRevB.84.235108>.
- ⁷³ Mikami, T. *et al.* Brillouin-wigner theory for high-frequency expansion in periodically driven systems: Application to floquet topological insulators. *Phys. Rev. B* **93**, 144307 (2016).
- ⁷⁴ Mori, T., Kuwahara, T. & Saito, K. Rigorous bound on energy absorption and generic relaxation in periodically driven quantum systems. *Phys. Rev. Lett.* **116**, 120401 (2016). URL <https://link.aps.org/doi/10.1103/PhysRevLett.116.120401>.
- ⁷⁵ Werner, P., Oka, T. & Millis, A. J. Diagrammatic monte carlo simulation of nonequilibrium systems. *Phys. Rev. B* **79**, 035320 (2009). URL <https://link.aps.org/doi/10.1103/PhysRevB.79.035320>.